Article

Superatomic-Charge-Density-Wave in Cluster-Assembled $Au_6Te_{12}Se_8$ Superconductors

Xu Chen, Ge Fei, Yanpeng Song, Tianping Ying,* Dajian Huang, Bingying Pan, Dongliang Yang,
Xiaofan Yang, Keyu Chen, Xinhui Zhan, Junjie Wang, Qinghua Zhang, Yanchun Li, Lin Gu,
Huiyang Gou, Xin Chen, Shiyan Li, Jinguang Cheng, Xiaobing Liu, Hideo Hosono, Jian-gang Guo,*
and Xiaolong Chen*

Read Online

ACCESS | Metrics & More | Article Recommendations | Supporting Information

ABSTRACT: Superatomic crystals are a class of hierarchical materials composed of atomically precise clusters assembled via van der Waals or covalent-like interactions. $Au_6Te_{12}Se_8$, an all-inorganic superatomic superconductor exhibiting superatomic-charge-density-wave (S-CDW), provides the first platform to study the response of its collective quantum phenomenon to the external pressure in superatomic crystals. We reveal a competition between S-CDW and superconductivity in an ultra-narrow pressure range. Distinct from conventional CDW ordering, S-CDW shows the lowest threshold (0.1 GPa) toward external pressure that is 1−2 orders of magnitude lower than other atomic compounds.

Prominently, a second superconducting phase emerges above 7.3 GPa with a threefold enhancement in the transition temperature (T_c) to 8.5 K, indicating a switch of the conduction channel from the a- to b-axis. In situ synchrotron diffractions and theoretical calculations reveal a pressure-mediated mesoscopic slip of the superatoms and a 2D-3D transition of the Fermi surface topology, which well explains the observed dimensional crossover of conductivity and re-entrant superconductivity.
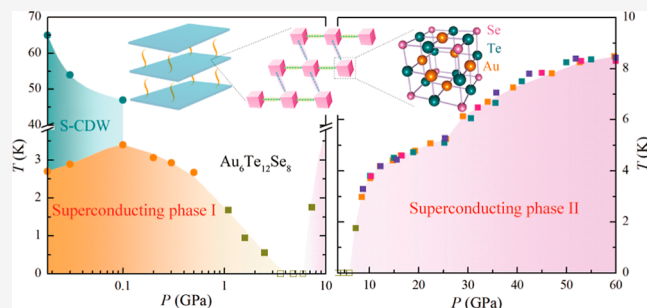
INTRODUCTION

Interatomic interactions such as van der Waals (vdW) force and ionic, covalent, and metallic bonds endow atomic solids with versatile but different properties.[1,2] The mesoscopic analogue of atomic solids, coined as the "superatomic crystal", is made up of strong-bonded atomic clusters connected through weak interactions within IIIA-VIA elements.[3−9] Known fullerenes,[10] Zintle ions,[11] and clusters of aluminum,[12] silicon,[13] boron,[14] and metal chalcogenide molecular clusters[15] are typical examples of superatoms. These superatomic clusters are believed to behave collectively as conventional single atoms with s-like, p-like, or d-like orbitals. Thus, hierarchical designs of the superatomic building blocks and their subsequent stacking sequence provide additional dimension to synthesize novel materials and discover emergent properties.[16]

Although the existence of superatoms has long been recognized, the study on superatomic crystals is burgeoning only recently. The electrical conductivity can be greatly altered by varying the mixture of different superatomic species.[17] Several interesting properties such as photoluminescence and electrochemical applications have been discovered.[18] As reported, the majority of superatomic crystals are diamagnetic semiconductors or insulators.[15] Thus far, the mediation of the bonding strength and material species mainly relies on self-assembling through organic capping ligands.[19] The use of

external tuning parameters to control and manipulate the inter-superatomic interactions remains an uncharted territory. The main challenge lies in how to tailor these clusters into crystals and how to probe the impact of intercluster interaction on their properties.

Only a handful of all-inorganic superatomic crystals have been reported.[20,21] The newly discovered $Au_6Te_{12}Se_8$ super-conductor (Figure 1) is composed of cubic blocks with identical chemical composition of six Au, twelve Te, and eight Se that are not shared with its adjacent unit cells.[22] Within the cubic block, Te atoms are nearest bonded by two Se atoms and four Au atoms to form a rigid cluster, as shown in Figure 1c. Given a strongly bonded cluster inside and the weakly bonded interactions in between clusters, $Au_6Te_{12}Se_8$ represents a standard superatomic crystal, where the $Au_6Te_{12}Se_8$ cluster behaves like a superatom. This material was initially discovered in our laboratory and later reported to be a natural mineral
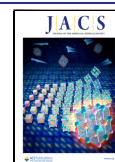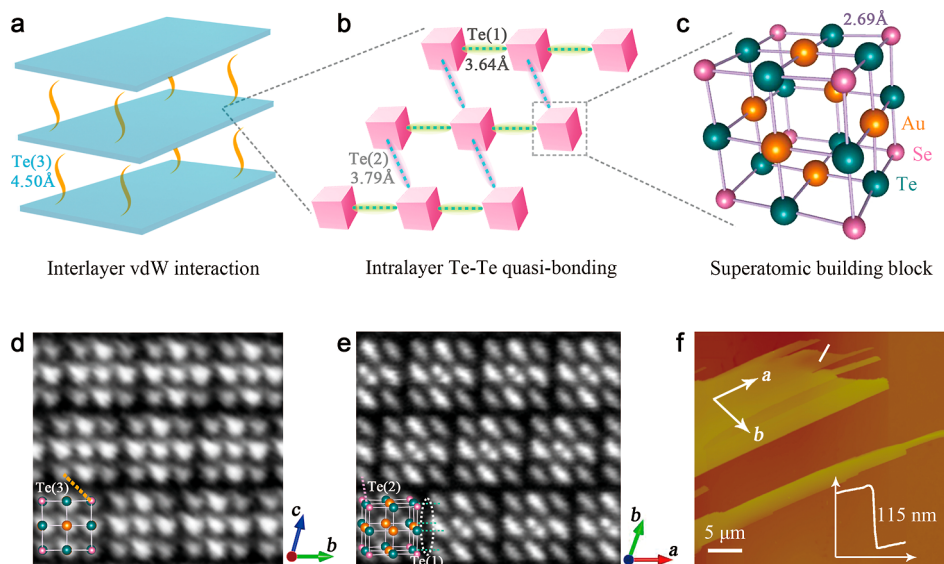
Figure 1. Heterogeneity of superatomic crystal $Au_6Te_{12}Se_8$. (a) Each van der Waals (vdW) layer is composed of arrays of woven superatoms. (b) Two sets of Te−Te quasi-bonds of 3.64 and 3.79 Å along the a-axis and b-axis, respectively. (c) Atomic cube with a composition of precise $Au_6Te_{12}Se_8$. Au, Te, and Se atoms are represented by golden, cyan, and pink balls, respectively. (d,e) Aberration-corrected scanning transmission electron microscopy micrographs along the a-axis and c-axis with its crystal structure superimposed. The Te···Te bundles are drawn in colors. (f) AFM topographic image of an exfoliated $Au_6Te_{12}Se_8$ flake. The inset shows the cross-sectional profile of the flake along the solid white line, giving a thickness of the flake of 115 nm. Note that we use Te(1) as a shorthand for the Te−Te(1) bond, and the same goes for other bonds.
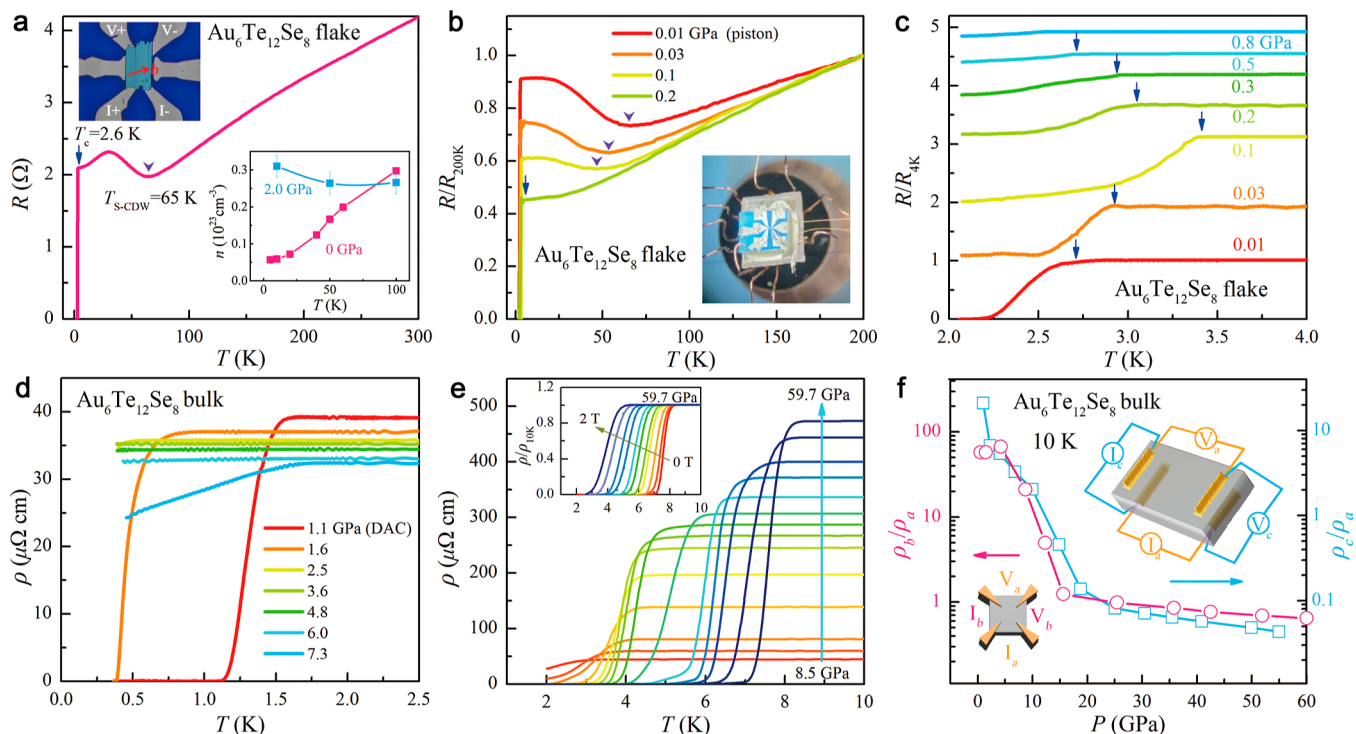

Figure 2. Evolution of S-CDW, superconductivity, and conducting anisotropy under pressure in $Au_6Te_{12}Se_8$. (a) Temperature-dependent resistance (R) of $Au_6Te_{12}Se_8$ thin flake at ambient pressure. The transition at 65 K (purple arrow) agrees well with the STM data.[24] The blue arrow shows the onset of superconductivity at 2.6 K. The upper inset shows the optical image of the fabricated device with the electrical current roughly along the b-axis. The lower inset shows the temperature-dependent carrier density (n) of $Au_6Te_{12}Se_8$ at 0 and 2.0 GPa. (b,c) Temperature-dependent normalized R below 1.0 GPa in different temperature ranges. Inset of (b) shows the setup of the device on the piston-cylinder apparatus. (d) Temperature-dependent resistivity (ρ) of $Au_6Te_{12}Se_8$ measured in the range of 1.1−7.3 GPa inside a DAC cell. (e) $\rho-T$ curves at a higher pressure of up to 59.7 GPa. Re-entrance of superconductivity is observed, accompanied by the monotonic increase in the normal state ρ (cyan arrow). ρ/ρ_{10K} under the external magnetic field at 59.7 GPa is shown in the inset. (f) Logarithmic plot of resistance ratios (ρ_b/ρ_a and ρ_c/ρ_a) as a function of pressure. The inset shows the electrode layout of ρ_a (orange), ρ_b (magenta), and ρ_c (blue) along the a-axis, b-axis, and c-axis, respectively.

found in the Koryak Highlands (Russia).[23] Very recently, scanning tunneling microscopy (STM) topographic observations revealed that the electronic states are strikingly different inside and outside the cubes, confirming that the $Au_6Te_{12}Se_8$ is a superatomic crystal.[24] The signature of charge modulation in the superatomic scale along the b-axis has been suggested, but a clear electronic transport evidence of superatomic-charge-density-wave (S-CDW) is still missing. On the other hand, CDW and superconductivity, as two kinds of electronic collective states, and their relationships have been intensively investigated in many atomic compounds, including $IrTe_2$, $ZrTe_3$, and CsV_3Sb_5.[25−29] The relationship in superatomic crystals, however, remains an unexplored territory.

High-pressure (HP) measurement, as a clean and feasible external tuning knob, has been widely used in the realm of atomic solids. In this work, we combine the nanofabrication and HP techniques and, for the first time, peek into the mutual interactions between the S-CDW and superconductivity. An interesting discovery is that the S-CDW order competes with superconductivity in an ultra-narrow pressure range and shows the lowest threshold of 0.1 GPa compared with conventional CDW compounds, which roots in the intrinsic bonding strength of Te−Te quasi-bonding that is much lower than other chemical bonds by 1−2 orders of magnitude. Superconductivity re-enters above 7.3 GPa, and T_cs increase steadily with the applied pressure until 59.7 GPa. The superatomic blocks are found to be intact while experiencing a crystallographic slip within the ab-plane by ($\sim$1/3 $\vec{a}$, $\sim$1/6 $\vec{b}$) at around 7.8 GPa. Concomitantly, pressure-driven re-entrant superconductivity and non-bonding to bonding transition between blocks are observed, which is accompanied by a switch of the conducting channel and Fermi surface topology from the a- to b-axis and the subsequent 2D to 3D crossover.

EXPERIMENTAL SECTION

Piston-Cylinder Measurements. Single-crystalline $Au_6Te_{12}Se_8$ was grown using the self-flux method, as described in ref 22. The high-angle annular-dark-field (HAADF) images were obtained using an ARM-200F (JEOL, Tokyo, Japan) scanning transmission electron microscope (STEM) operated at 200 kV with a CEOS Cs corrector (CEOS GmbH, Heidelberg, Germany) to cope with the probe-forming objective spherical aberration. The attainable resolution of the probe defined by the objective pre-field is 78 picometers. The focused ion beam (FIB) method was used to cut the narrow sample (width: $\sim$50 nm and thickness 20−50 μm) for structural analysis. We prepared the few-layer $Au_6Te_{12}Se_8$ sample by exfoliating thin flakes from a bulk crystal using scotch tape and transferring onto the SiO_2 (280 nm)/Si substrate by the polydimethylsiloxane (PDMS) method. The thickness of the flake was determined by atomic force microscopy (AFM, Bruker Multimode 8).The fabricated device was then sealed in a Teflon cell filled with glycerin as the pressure-transmitting medium (PTM). A piece of Sn wire was used as a manometer.

High-Pressure Measurements. In situ HP electrical transport of the $Au_6Te_{12}Se_8$ single crystal was measured in the physical property measurement system (PPMS, Quantum Design) and a ^{3}He cryostat using a diamond anvil cell (DAC) with a facet diameter of 300 μm. We used three different configurations of the electrodes to measure the electrical transport properties along ρ_a, ρ_b, and ρ_c (see the insets of Figure 2f). The cubic boron nitride (cBN) powders were employed as pressure transmitting medium and insulating material. Before and after each run, the pressure was measured using the ruby fluorescence method. In situ HP Raman spectra (Horiba, Lab-RAM HR revolution) were recorded at room temperature. In situ high-P synchrotron powder XRD experiments were performed at the 4W2 station of the Beijing Synchrotron Radiation facility (BSRF) with a wavelength of 0.6199 Å (20 keV) and a spot size of 35 μm × 12 μm.

Theoretical Calculations. Structural relaxation and electronic calculations were performed using density functional theory (DFT) within the Perdew−Burke−Ernzerhof (PBE)[35] exchange−correlation and generalized gradient approximation (GGA) functional as implemented in the Vienna *Ab initio* Simulation Package (VASP) code.[36] The lattice parameters and atomic positions were fully relaxed without any symmetry constraints. The all-electron projector-augmented wave approach was adopted with a plane-wave cutoff of 500 eV, and Monkhorst−Pack[37] k-meshes with a grid spacing of $2\pi \times 0.02$ Å^{-1} were used to achieve a good convergence for the enthalpy.

RESULTS AND DISCUSSION

Assembly of Multiatom Clusters $Au_6Te_{12}Se_8$. The isolated superatomic building blocks can be clearly seen and isolated from one another in the atomic-resolution images of $Au_6Te_{12}Se_8$ from both the side view (Figure 1d) and top view (Figure 1e). These building blocks are woven together by anisotropic Te−Te quasi-bonding into 2D sheets with Te(1) and Te(2) bond lengths of 3.64 and 3.79 Å, respectively, and then by vdW interaction along the c-axis with a Te(3) bond length of 4.50 Å. Because of the vdW nature in the c direction and the somewhat longer bond length and less bonding strength along the b-axis, $Au_6Te_{12}Se_8$ can be easily exfoliated into ribbon shape with clearly defined crystallographic directions (Figure 1f). It is also worth noting that the exfoliated thin flakes are quite stable against moisture for more than 5 years in our laboratory, which highlights the robustness of this superatomic compound and facilitates various future investigations.

Evolution of S-CDW, Superconductivity, and Conducting Anisotropy under Pressure. As shown in Figure 2a, a resistance upturn is clearly seen at 65 K in $Au_6Te_{12}Se_8$ when measured along the b-axis but is absent along the a-axis, indicating a gap opening on the partial Fermi surface due to the anisotropic electronic structures. This is consistent with the STM observation of a superatomic-size charge modulation along the b-axis[24] and thus provides direct evidence of S-CDW transition. We then trace the evolution of S-CDW and superconductivity of the thin flake in the low-pressure region using a piston-cylinder apparatus (0−2 GPa) with details included in the Experimental Section. It can be seen that the S-CDW is suppressed by external pressure, accompanied by the increase in T_c, see Figure 2b,c. As the S-CDW disappears, the T_c reaches its maximum of 3.4 K and then gradually decreases. The carrier density of $Au_6Te_{12}Se_8$ at ambient pressure and 2.0 GPa is summarized in the lower inset of Figure 2a. As anticipated, the ambient carrier density shows a kink at around 65 K, indicating the opening of the CDW gap on the partial Fermi surface along the b-axis. When the CDW order is quenched by external pressure (the 2.0 GPa curve), the loss of electrons can no longer be observed. The slight upturn at the lower temperature may be caused by the deformation of the sample under pressure. These behaviors are similar to those in conventional compounds, indicating that superatomic materials can be viewed as a mesostructural version of atomic materials not only from the electronic point of view (shared electrons within the building blocks according to the STM results[24]) but also based on the evolution of collective quantum states (the competition of S-CDW and superconductivity).

We further check its transport property under higher pressures using the diamond anvil cell (DAC) apparatus, see details in the Experimental Section. As shown in Figures 2d and S1−S5, the superconducting transition is suppressed above
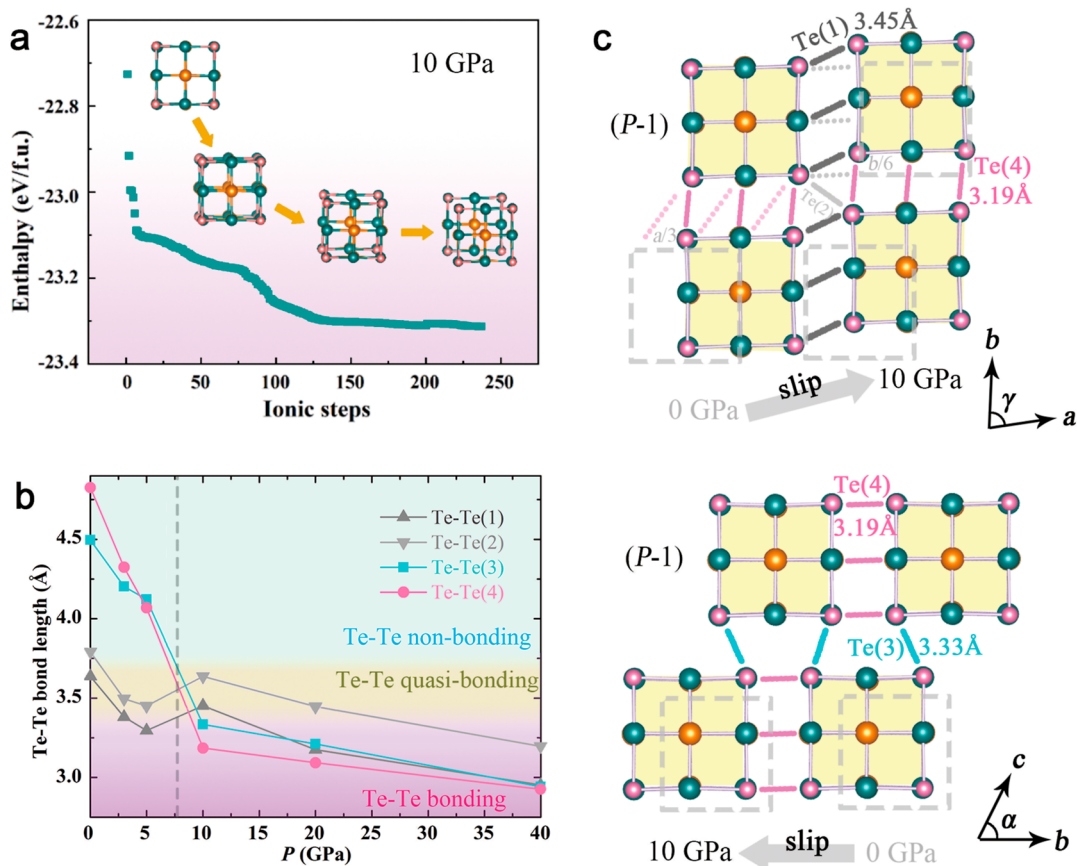
Figure 3. Structural evolution of superatomic crystal $Au_6Te_{12}Se_8$ under external pressure. (a) Evolution of enthalpy of ionic steps during the ionic relaxation in $Au_6Te_{12}Se_8$ at 10 GPa. All the lattice constants and atomic coordinates were fully relaxed to generate a stable structure under high pressure. From 0 to 5 GPa, there is no structural slip, maintaining the ambient structure. (b) Pressure-dependence of four Te−Te distances extracted from theoretical calculations shown in (a). (c) Illustration of structure transition at ambient pressure and 10 GPa. A slip of the superatomic array is schematically drawn. The initial position is depicted in gray dashed squares. Bonds along each crystalline axis are painted in color with reference to (b).

2.5 GPa and cannot be observed at 3.6−6.0 GPa down to 0.4 K. Above 7.3 GPa, we observe a re-entrant superconductivity. Zero resistance is achieved at a pressure of 12.2 GPa (Figure 2e). The onset T_c increases to 8.5 K at 59.7 GPa, which is three times higher than the initial T_c of 2.8 K at ambient pressure. Note that the two superconducting phases are separated by 2.4 GPa above 0.4 K. The $\rho-T$ curves of the re-entrant superconductivity under different magnetic fields are shown in the inset of Figure 2e, from which we acquire its upper critical field H_{c2} = 3.5 T. Although re-entrant superconductivity has been discovered in a variety of compounds, including $K_xFe_{2-y}Se_2$ and CsV_3Sb_5,[30−32] this is first observed in a superatomic crystal. Figures 2f, S6, and S7 show the pressure-dependent ρ_b/ρ_a and ρ_c/ρ_a at 10 K and other temperatures, respectively. The ρ_b/ρ_a ratios decrease from 65 to ∼0.6 when the external pressure is increased from 0.8 to 50 GPa; meanwhile, the ρ_c/ρ_a ratios decrease from 11 to ∼0.05, suggesting that the re-entrant bulk superconductivity is accompanied by a change in the conducting channel from 2D (quasi-1D) to 3D.

Structural Evolution under External Pressure. Since $Au_6Te_{12}Se_8$ can be easily exfoliated into ribbon-like thin flakes with edges along the a and b directions (Figures 1f and S8), it indicates the existence of appreciable in-plane interactions. Taking the ambient structure as the initial model, we predicted the structures under high pressures by DFT calculations.

Figure 3a depicts the enthalpy of ionic steps of $Au_6Te_{12}Se_8$ at 10 GPa, and the superimposed images are the relaxed structures, illustrating the lattice evolution process. At each step of the atomic relaxation, the self-consistent calculations of electrons were carried out. With the gradual convergence of energy and force, the superatoms glide along the b- and c-axes. At the same time, the enthalpy of $Au_6Te_{12}Se_8$ reaches its favorite value. We performed the same procedure for 0, 3, 5, 10, 20, and 40 GPa and summarized the pressure-dependent intercube Te−Te distances in Figure 3b. The Te(1) and Te(2) decrease with increasing pressure, and both bond lengths jump a little at 5−10 GPa but still lie in the Te−Te quasi-bonding region. Meanwhile, the Te(3) and Te(4) go through a non-bonding to bonding transition and an abrupt lattice collapse. The pressure of structural transition agrees well with the onset pressure at which the second superconducting phase emerges.

This non-bonding to bonding transition can be attributed to a slip of the blocks mainly within the ab-plane by a vector of ($\sim 1/3\ \vec{a}$, $\sim 1/6\ \vec{b}$) as a response to the applied pressures, as shown in Figures 3c and S9. The dashed broken square (0 GPa) and the solid structures (10 GPa) illustrate a pressure-induced first-order transition, while its space group remains $P\bar{1}$. As labeled in Figure 3c and the trend depicted in Figure 3b, the shortest Te(1) bond along the a-axis at ambient pressure is now the longest at 3.45 Å, while the longest Te(4) bond along the b-axis becomes the shortest at 3.19 Å under 10 GPa. Thus,
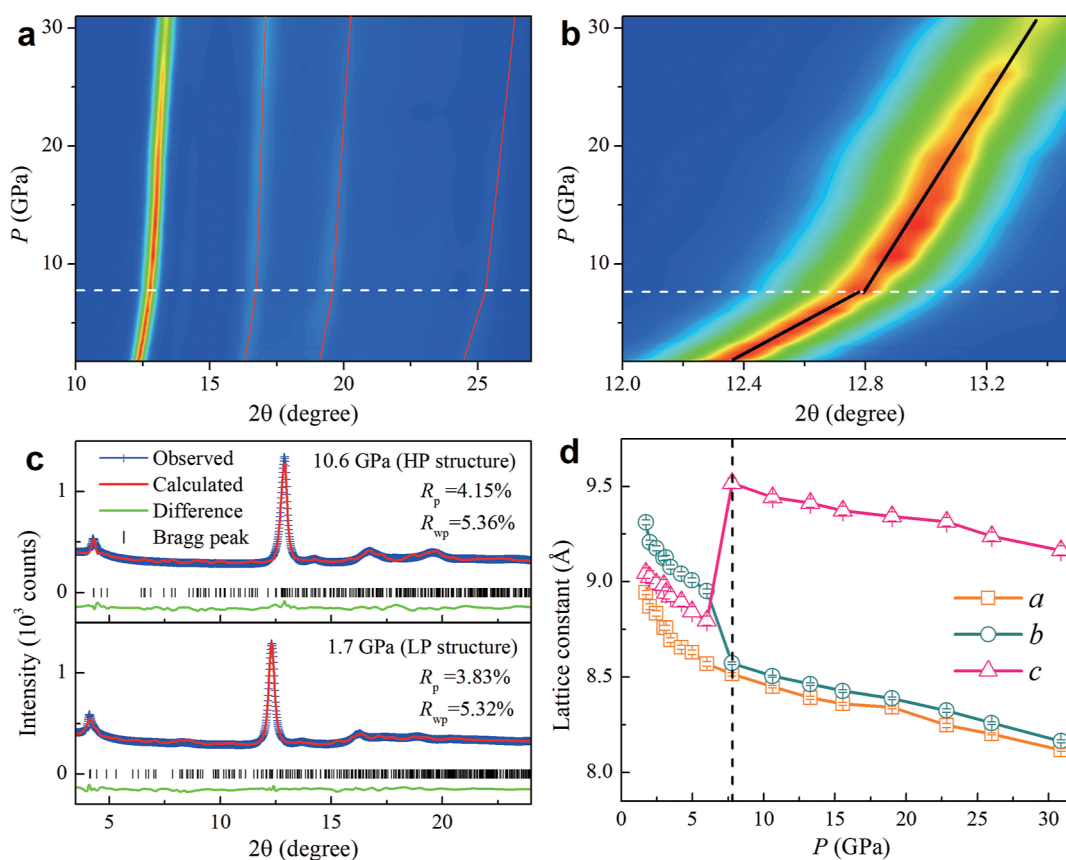
Figure 4. Synchrotron diffraction patterns of $Au_6Te_{12}Se_8$ under pressure. The color contour in the range of $10-27.5°$ (a) and $12-13.5°$ (b). (c) Rietveld refinements of the diffraction pattern at 1.7 GPa and 10.6 GPa using the theoretical predicted low-pressure (LP) and high-pressure (HP) structures, respectively. (d) Evolution of lattice parameters with the variation of external pressure. The broken lines shown in (a,b,d) highlight a critical pressure of 7.8 GPa.

the aforementioned channel transition in conductivity shown in Figure 2f is satisfactorily explained by this reversion in bond length. To visualize this non-bonding to bonding transition, we further calculated the electron location function (ELF) at ambient pressure and 10 GPa (Figure S10). 0.5 and 1 are the indicators of covalent and ionic bonds, respectively.[33] A high density of electrons can be observed within a single $Au_6Te_{12}Se_8$ cube with an ELF value of 0.6, which is much higher than that of 0.11 in between the cubes. It means that the superatomic features survive under pressures. At ambient pressure, the intercubic Te−Te interactions are mainly along the a-axis. At 10 GPa, however, electrons are confined within the intercubic Te−Te bonds along the b-axis, see Figure S10. Such a charge redistribution along different crystallographic axes is caused by the formation of the pressure-induced quasi-bonding state.

Experimental evidence of the structure information is essential to verify the theoretical predictions. Therefore, using synchrotron X-ray diffractions data under 1.7−30.9 GPa, we conducted a thorough investigation of structural evolution under external pressure (Figure S11). The ambient-pressure structure of $Au_6Te_{12}Se_8$ was determined by our group[22] and confirmed by another group.[23] The evolution of the structure under pressure is obtained through the analysis of the diffraction patterns using the Rietveld refinements.

We further map the color contour plot of these diffraction patterns in Figure 4a, along with the primary diffraction peaks enlarged in Figure 4b. Interestingly, all of the diffraction peaks exhibit kinks at 7.8 GPa, which is consistent with our

theoretical prediction of structural slip at 5−10 GPa and experimentally re-entrant superconductivity at 7.3 GPa. Figure 4c shows the Rietveld refinements of two typical diffraction patterns using the theoretically predicted structure as the starting model. We fix the atom positions in the distorted $Au_6Te_{12}Se_8$ cube and only refine the lattice constants of the unit cell. For the pattern collected at 10.6 GPa, we refine the pattern based on the HP structure model and obtain agreement factors $R_p = 4.15\%$ and $R_{wp} = 5.36\%$. In comparison, the refinement based on the ambient structure model leads to large values of $R_p = 6.39\%$ and $R_{wp} = 9.46\%$. It indicates that the structure after slip, that is, HP crystal structure, fits the diffraction patterns better.

The refined pressure-dependent lattice constants are plotted in Figure 4d. The sharp jump in the lattice parameter c and the continual decrease in parameters a and b agree well with the theoretical ones shown in Figure S12. Therefore, the proposed structure slip is now verified theoretically and experimentally. The slip of entire $Au_6Te_{12}Se_8$ building blocks is reminiscent of behavior observed in materials such as Nb_3Cl_8.[38]

Phase Diagram of $Au_6Te_{12}Se_8$. The phase diagrams of $Au_6Te_{12}Se_8$ over the entire pressure range are plotted in Figure 5. The delicate competing nature between S-CDW and superconductivity in an ultra-narrow pressure region is mapped in Figure 5a. After the first superconducting phase is completely suppressed, a non-superconducting ground state between 3.6 and 6 GPa is identified. It is very likely that a quantum-critical-point may exist between the two super-
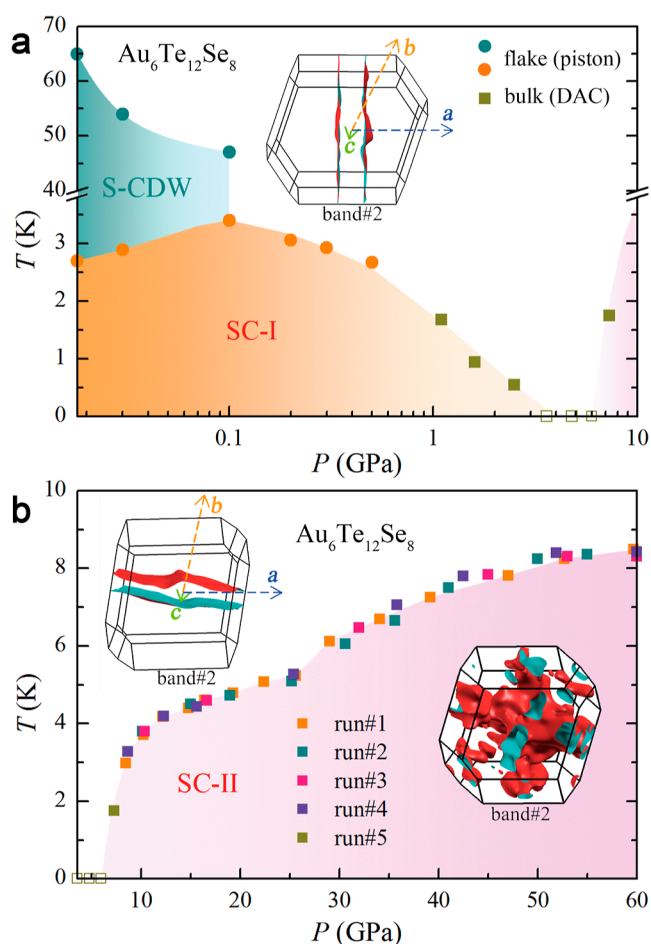
Figure 5. S-CDW, superconductivity, and Fermi surface topology in pressurized $Au_6Te_{12}Se_8$. (a) Phase diagram of $Au_6Te_{12}Se_8$ at low pressure. The inset shows the dominated band#2 at ambient pressure in the first Brillouin zone. (b) Re-entrant superconductivity of $Au_6Te_{12}Se_8$ in the higher pressure region. Insets show the conducting channel along the *b*-axis and 3D Fermi surface at 10 and 60 GPa, respectively. Detailed description of the band structure and Fermi surface can be found in SI.

conducting phases and is worth further investigations. Above 7.3 GPa, a second superconducting phase shows up, see Figure 5b. We noted that our T_c in $Au_6Te_{12}Se_8$ is totally different from the pressure response in pure elemental Te, ruling out the possibility of impurity. Besides, the $Au_6Te_{12}Se_8$ does not decompose during measurements, as evidenced by the identical Raman spectra of the pristine and pressurized sample, see Figure S13. For the evolution of the Fermi surface, these quasi-2D Fermi surfaces first gradually develop in the perpendicular direction with increasing pressures, in line with the superatomic slip of 5−10 GPa, the channel switch in conductivity, and bond lengths. As the pressure further increases, the Fermi surface eventually changes into 3D geometry at 60 GPa.[34] The insets of Figures 5, S14, and S15 clearly show these variations.

DISCUSSION

The pressure-dependent structure and transport properties of $Au_6Te_{12}Se_8$ exhibit new features distinct from the atomic crystals. The rigid superatomic building blocks can undergo crystallographic slips, resulting in a non-bonding to bonding transition in intercube Te−Te bonds. Upon applying high-

enough pressures, for example, 60 GPa, the crystal transforms from 2D to 3D (Figure S10). In terms of transport properties, the anisotropic ratio of ρ_c/ρ_a decreases by 3 orders of magnitude, confirming the 2D−3D crossover in the electronic structures. The emergence of the second superconducting phase and threefold enhancement of T_c should be related to the enhancement of density of states, as shown in Figure S16. Herein, the relationship between the structure and transport property is established in superatomic $Au_6Te_{12}Se_8$.

We mention that this competition is not a simple resemblance to the atomic CDW ordering. Quantitatively, the superatomic-CDW (S-CDW) is completely suppressed at a pressure of 1∼2 orders of magnitude (0.1 GPa) lower than that for conventional atomic superconductors (a full list of pressure-quenching CDW thresholds can be found in Table S1). Canonical CDW involves the shifts of atoms following the formation of the periodic density of electrons along one or more directions, while the superatomic CDW entails the slip of the entire $Au_6Te_{12}Se_8$ building blocks. Additionally, the electron can be polarized within one cube to create a distinct "antipolar state" that conventional CDW will not have.[24] Therefore, apart from charge and spin, polarization caused by a Jahn−Teller-type distortion within superatomic units can thus serve as another degree of freedom that steps in to modulate the properties in a mesoscopic level.

CONCLUSIONS

In conclusion, we observe a direct competition between S-CDW and superconductivity at a superatomic level for the first time. The S-CDW shows the lowest pressure threshold compared to that of CDW in conventional atomic compounds, which should be an intrinsic property for superatomic crystals. The emergence of the second superconducting phase is accompanied by crystallographic slip of superatomic blocks, rather than changing the geometry or bonding environments within a single block. The whole superatom cluster, therefore, can be treated like a single atom because of the existence of soft quasi-bonds. The ultra-sensitive pressure response stems from the weak bonding among superatoms, suggesting that superatomic materials may need a much smaller energy scale to change their crystal and electronic structures than their monoatomic counterparts. As a fundamental building unit, superatoms may be used to simulate the interactions in atomic compounds and design more compounds with hierarchical structures in chemistry. These results extend our knowledge of the correlation among S-CDW, superconductivity, and structural phase transition in a new class of materials, superatomic compounds. This work significantly modifies physical features in superatomic crystals that have already been identified and will boost the hierarchical design and assembly of novel superatomic superconductors.

ASSOCIATED CONTENT

Supporting Information

The Supporting Information is available free of charge at https://pubs.acs.org/doi/10.1021/jacs.2c09499.

> Full list of pressure-quenching CDW thresholds, pressure-dependent electrical transport measurements for different runs, optical image of the exfoliated flakes, crystal slip under pressure, valence electron localization function under pressure, synchrotron X-ray diffraction patterns and lattice constants of $Au_6Te_{12}Se_8$ at different

pressures, Raman spectrum before and after *in situ* pressure measurements, and bands and Fermi surface of $Au_6Te_{12}Se_8$ at different pressures (PDF)

■ AUTHOR INFORMATION

Corresponding Authors

Tianping Ying − *Beijing National Laboratory for Condensed Matter Physics, Institute of Physics, Chinese Academy of Sciences, Beijing 100190, China;* ⊙ orcid.org/0000-0001-7665-1270; Email: ying@iphy.ac.cn

Jian-gang Guo − *Beijing National Laboratory for Condensed Matter Physics, Institute of Physics, Chinese Academy of Sciences, Beijing 100190, China; Songshan Lake Materials Laboratory, Dongguan 523808, China;* ⊙ orcid.org/0000-0003-3880-3012; Email: jgguo@iphy.ac.cn

Xiaolong Chen − *Beijing National Laboratory for Condensed Matter Physics, Institute of Physics, Chinese Academy of Sciences, Beijing 100190, China; School of Physical Sciences, University of Chinese Academy of Sciences, Beijing 100049, China; Songshan Lake Materials Laboratory, Dongguan 523808, China;* ⊙ orcid.org/0000-0001-8455-2117; Email: chenx29@iphy.ac.cn

Authors

Xu Chen − *Beijing National Laboratory for Condensed Matter Physics, Institute of Physics, Chinese Academy of Sciences, Beijing 100190, China;* ⊙ orcid.org/0000-0003-3477-2204

Ge Fei − *Laboratory of High Pressure Physics and Material Science (HPPMS), School of Physics and Physical Engineering, Qufu Normal University, Qufu 273100, China*

Yanpeng Song − *Beijing National Laboratory for Condensed Matter Physics, Institute of Physics, Chinese Academy of Sciences, Beijing 100190, China*

Dajian Huang − *Center for High Pressure Science and Technology Advanced Research (HPSTAR), Beijing 100094, China*

Bingying Pan − *School of Physics and Optoelectronic Engineering, Ludong University, Yantai 264025, China;* ⊙ orcid.org/0000-0001-9813-5103

Dongliang Yang − *Beijing Synchrotron Radiation Facility Institute of High Energy Physics, Chinese Academy of Sciences, Beijing 100049, China*

Xiaofan Yang − *State Key Laboratory of Surface Physics, Department of Physics, and Laboratory of Advanced Materials, Fudan University, Shanghai 200433, China*

Keyu Chen − *Beijing National Laboratory for Condensed Matter Physics, Institute of Physics, Chinese Academy of Sciences, Beijing 100190, China*

Xinhui Zhan − *Laboratory of High Pressure Physics and Material Science (HPPMS), School of Physics and Physical Engineering, Qufu Normal University, Qufu 273100, China*

Junjie Wang − *Beijing National Laboratory for Condensed Matter Physics, Institute of Physics, Chinese Academy of Sciences, Beijing 100190, China; School of Physical Sciences, University of Chinese Academy of Sciences, Beijing 100049, China*

Qinghua Zhang − *Beijing National Laboratory for Condensed Matter Physics, Institute of Physics, Chinese Academy of Sciences, Beijing 100190, China*

Yanchun Li − *Beijing Synchrotron Radiation Facility Institute of High Energy Physics, Chinese Academy of Sciences, Beijing 100049, China*

Lin Gu − *Beijing National Laboratory for Condensed Matter Physics, Institute of Physics, Chinese Academy of Sciences, Beijing 100190, China;* ⊙ orcid.org/0000-0002-7504-031X

Huiyang Gou − *Center for High Pressure Science and Technology Advanced Research (HPSTAR), Beijing 100094, China*

Xin Chen − *Laboratory of High Pressure Physics and Material Science (HPPMS), School of Physics and Physical Engineering, Qufu Normal University, Qufu 273100, China;* ⊙ orcid.org/0000-0003-0652-0798

Shiyan Li − *State Key Laboratory of Surface Physics, Department of Physics, and Laboratory of Advanced Materials, Fudan University, Shanghai 200433, China*

Jinguang Cheng − *Beijing National Laboratory for Condensed Matter Physics, Institute of Physics, Chinese Academy of Sciences, Beijing 100190, China;* ⊙ orcid.org/0000-0002-4969-1960

Xiaobing Liu − *Laboratory of High Pressure Physics and Material Science (HPPMS), School of Physics and Physical Engineering, Qufu Normal University, Qufu 273100, China;* ⊙ orcid.org/0000-0002-0680-1947

Hideo Hosono − *Materials Research Center for Element Strategy, Tokyo Institute of Technology, Midori, Yokohama 226-8503, Japan;* ⊙ orcid.org/0000-0001-9260-6728

Complete contact information is available at:
https://pubs.acs.org/10.1021/jacs.2c09499

Notes

The authors declare no competing financial interest.

■ ACKNOWLEDGMENTS

■ REFERENCES

(1) Yokoya, T.; et al. Fermi surface sheet-dependent superconductivity in 2H-NbSe$_2$. *Science* **2001**, *294*, 2518.

(2) Xiao, D.; et al. Coupled spin and valley physics in monolayers of MoS$_2$ and other group-VI dichalcogenides. *Phys. Rev. Lett.* **2012**, *108*, 196802.

(3) Bergeron, D. E.; Castleman, A. W., Jr.; Morisato, T.; et al. Formation of Al$_{13}$I$^-$: evidence for the superhalogen character of Al$_{13}$. *Science* **2004**, *304*, 84.

(4) Bergeron, D. E.; Roach, P. J.; Castleman, A. W., Jr.; et al. Al cluster superatoms as halogens in polyhalides and as alkaline earths in iodide salts. *Science* **2005**, *307*, 231.

(5) Roy, X.; Lee, C. H.; Crowther, A. C.; et al. Nanoscale atoms in solid-state chemistry. *Science* **2013**, *341*, 157.

(6) Reveles, J. U.; Khanna, S.; Roach, P.; et al. Multiple valence superatoms. *Proc. Natl. Acad. Sci. U.S.A.* **2006**, *103*, 18405.

(7) Doud, E. A.; et al. Superatoms in materials science. *Nat. Rev. Mater.* **2020**, *5*, 371.

(8) Li, Y.; et al. Double-helical assembly of heterodimeric nanoclusters into supercrystals. *Nature* **2021**, *594*, 380.

(9) Castleman, A. W., Jr.; Jena, P. Clusters: a bridge across the disciplines of environment, materials science, and biology. *Proc. Natl. Acad. Sci. U.S.A.* **2006**, *103*, 10554.

(10) Canning, A.; Galli, G.; Kim, J. Carbon Superatom Thin Films. *Phys. Rev. Lett.* **1997**, *78*, 4442.

(11) Zhao, J.; Feng, M.; Yang, J.; Petek, H. The superatom states of fullerenes and their hybridization into the nearly free electron bands of fullerites. *ACS Nano* **2009**, *3*, 853.

(12) Castleman, A. W.; Khanna, S. N. Clusters, superatoms, and building blocks of new materials. *J. Phys. Chem. C* **2009**, *113*, 2664.

(13) Jena, P. Beyond the periodic table of elements: the role of superatoms. *J. Phys. Chem. Lett.* **2013**, *4*, 1432.

(14) Hu, S.; et al. Nearly free electron superatom states of carbon and boron nitride nanotubes. *Nano. Lett.* **2010**, *10*, 4830.

(15) Yang, J. J.; et al. Superatomic solid solutions. *Nat. Chem.* **2021**, *13*, 607.

(16) Xie, W.; et al. Magnetic coupling induced self-assembly at atomic level. *Chin. Phys. Lett.* **2019**, *36*, 116401.

(17) Cui, X.; et al. Realizing nearly-free-electron like conduction band in a molecular film through mediating intermolecular van der waals interactions. *Nat. Commun.* **2019**, *10*, 3374.

(18) Stoica, V. A.; et al. Optical creation of a supercrystal with three-dimensional nanoscale periodicity. *Nat. Mater.* **2019**, *18*, 377.

(19) Voevodin, A.; et al. Multifunctional vesicles from a self-assembled cluster-containing diblock copolymer. *J. Am. Chem. Soc.* **2018**, *140*, 5607.

(20) Fischer, C.; et al. Crystal structure and thermodynamic analysis of the new semiconducting chevrel phase $Re_6S_8C_{12}$. *Ber. Bunsen-Ges.* **1992**, *96*, 1652.

(21) Speziali, N. L.; et al. Single crystal growth, structure and characterization of the octahedral cluster compound $Re_6Se_8Br_{12}$. *Mater. Res. Bull.* **1988**, *23*, 1597.

(22) Guo, J. G.; et al. Quasi-two-dimensional superconductivity from dimerization of atomically ordered $AuTe_2Se_{4/3}$ cubes. *Nat. Commun.* **2017**, *8*, 871.

(23) Tolstykh, N. D.; et al. Maletoyvayamite, $Au_3Se_4Te_6$, a new mineral from Maletoyvayam deposit, Kamchatka peninsula, Russia. *Mineral. Mag.* **2020**, *84*, 117.

(24) Xing, S. Y. et al. Emerging correlated charge orders in a layered super-atomic crystal. **2021**,arxiv:2110.09058 (accepted by Phys.-Rev.X).

(25) Oh, Y. S.; et al. Anionic Depolymerization transition in $IrTe_2$. *Phys. Rev. Lett.* **2013**, *110*, 127209.

(26) Yomo, R.; et al. Pressure effect on competition between charge density wave and superconductivity in $ZrTe_3$: Appearance of pressure-induced reentrant superconductivity. *Phys. Rev. B: Condens. Matter Mater. Phys.* **2005**, *71*, 132508.

(27) Song, Y. P.; et al. Competition of superconductivity and charge density wave in selective oxidized CsV_3Sb_5 thin flakes. *Phys. Rev. Lett.* **2021**, *127*, 237001.

(28) Chen, K. Y.; et al. Double superconducting dome and triple enhancement CsV_3Sb_5 under high pressure. *Phys. Rev. Lett.* **2021**, *126*, 247001.

(29) Yu, F. H.; et al. Unusual competition of superconductivity and charge-density-wave state in a compressed topological kagome metal. *Nat. Commun.* **2021**, *12*, 3645.

(30) Sun, L. L.; et al. Re-emerging superconductivity at 48 kelvin in iron chalcogenides. *Nature* **2012**, *483*, 67.

(31) Chen, X.; et al. Highly robust reentrant superconductivity in CsV_3Sb_5 under Pressure. *Chin. Phys. Lett.* **2021**, *38*, 057402.

(32) Zhao, C. C.; et al. Nodal superconductivity and super-conducting domes in the topological Kagome metal CsV3Sb5. **2021**, arxiv:2102.08356, .

(33) Ma, Y.; et al. Transparent dense sodium. *Nature* **2009**, *457*, 182.

(34) Yu, F. H.; et al. Pressure-induced dimensional crossover in a Kagome superconductor. *Phys. Rev. Lett.* **2022**, *128*, 077001.

(35) Perdew, J. P.; Burke, K.; Ernzerhof, M. Generalized gradient approximation made simple. *Phys. Rev. Lett.* **1996**, *77*, 3865.

(36) Kresse, G.; Furthmüller, J. Efficiency of ab-initio total energy calculations for metals and semiconductors using a plane-wave basis set. *Comput. Mater. Sci.* **1996**, *6*, 15.

(37) Monkhorst, H. J.; Pack, J. D. Special points for Brillouin-zone integrations. *Phys. Rev. B: Solid State* **1976**, *13*, 5188.

(38) Haraguchi, Y.; et al. Magnetic−nonmagnetic phase transition with interlayer charge disproportionation of Nb_3 trimers in the cluster compound Nb_3Cl_8. *Inorg. Chem.* **2017**, *56*, 3483.

⧉ Recommended by ACS